

Landslides (2020) 17:1353–1361
 DOI 10.1007/s10346-019-01337-x
 Received: 23 July 2019
 Accepted: 18 December 2019
 Published online: 30 January 2020
 © Springer-Verlag GmbH Germany
 part of Springer Nature 2020

Xiuqiang Bai · Siming He

Dynamic process of the massive Aru glacier collapse in Tibet

Abstract Due to global climatic warming, the possibility of collapse of polythermal glaciers is increasing. In the summer of 2016, two massive glaciers suddenly collapsed at Aru Village, Ali District, Xizang Autonomous Region, China, running out up to 7 km and killing nine herders. These events occurred suddenly in a remote area, and quantitative data about them was difficult to obtain quickly. Their seismic waves, however, could be quickly inverted to estimate the event motion parameters; the inversion results reflecting the average state. In order to have an initial judgment on the deposit range and the kinematic parameters at different positions after the collapse, seismic-wave inversions were used to estimate parameters (e.g., mass and friction coefficient) for numerical simulation to quickly simulate the motion processes that are important for the initial rescue, especially in the absence of topographic data. Numerical simulation showed that even though the shape and depth of the source area as assigned from such inversion were slightly different from the real situation, the effect on the final deposit morphology was not so great, which can be used as a reference for useful assessment after future disasters.

Keywords Aru ice avalanches · Seismic wave inversion · Numerical analysis · Natural terrain

Introduction

With continuing global warming, the environment in which we live is experiencing great changes, especially in polar regions and the Qinghai-Tibet Plateau (Liu and Chen 2000; Wang et al. 2008; Duan and Xiao 2015) (Fig. 1). The most obvious features are melting ice sheets, ice-shelf collapses, and the occurrence of ice avalanches, which may cause sea level rise, casualties, and property loss. Compared with the large reserves of glaciers in the polar-regions, mountain glaciers are more sensitive to climate change. Large ice avalanches, rock avalanches, and mixed events are well documented for the glaciated regions in the world (McSaveney 2002; Kääb et al. 2005; Schneider 2004; Sosio et al. 2008; Tian et al. 2017). Most of them are located in high mountains or sparsely populated areas, and have such destructive power that field measurements relevant to their dynamics are scarce.

Characterizing the dynamics of ice-rock avalanches is important for our understanding of the mechanical properties of the flowing material and for the prediction of the velocity and runout extent of rapid ice-rock avalanches (Favreau et al. 2010), which will help us to establish protective structures in their potential motion paths to reduce damage to people and property in future geological disasters. Important information about their motion process is recorded in the seismic signals generated by the gravitational mass flows during their emplacement. Using the seismic stations around them, these seismic signals can be used to estimate collapsed mass, dynamics, and mechanical behavior (friction coefficient, velocity, momentum,

etc.) (Brodsky et al. 2003; Huggel et al. 2007; Cole et al. 2009; Favreau et al. 2010; Moretti et al. 2012, 2015; Li et al. 2017; Bai et al. 2019; Dufresne et al. 2019; Li et al. 2019). Seismic wave inversion is a way to analyze flow dynamics and provide parameters for study in numerical simulation. The kinematic parameters of mass flows inverted by seismic waves however are average states. Therefore, it is necessary to also study the mass flow dynamics in numerical simulation (Sabot et al. 1998; Favreau et al. 2010; Schneider et al. 2010; Moretti et al. 2012, 2015; Yamada et al. 2016).

Immediately an ice avalanche happens, we need to know the size and scale of the disaster. Seismic wave inversion can be used to estimate the mass and provide parameters for numerical simulation to reproduce the motion process. Numerical simulation is an important method to calculate the gravitational mass flow dynamics, runout, and deposition, which can be employed for the investigation and back analysis of past events. In this study, we use seismic records and numerical simulation to explore the dynamics of the 2016 Aru-1 and Aru-2 ice avalanches, which happened at the Aru Range in the western Tibetan Plateau. In addition, according to the Aru-1 and Aru-2 avalanches, horizontal distances (L), drop heights (H), and the durations of ice avalanche movement inferred from seismic waves signals generated by its momentum changes; we can deduce that the ice avalanche process exhibits high speed and low friction during the movement. The factors that cause the friction coefficient to decrease may be entrainment (McDougall and Hungr 2005), fragmentation (Davies et al. 1999; McSaveney and Davies 2007), avalanche volume, water and ice content, friction surface, and topography (Schneider et al. 2011). Considering that these factors may affect the Aru avalanches movement process, we embed these influence factors into the dynamic simulation model.

Setting and characteristics of Aru avalanches

A huge mass of glacier first collapsed (termed Aru-1) at 11:15 (Beijing time, UTC+8), on 17 July 2016, from the lower part (5800–5190 m a.s.l.) of the Aru Glacier (34.03°N; 82.25°E) that ranges from 5250 to 6150 m a.s.l. The collapsed ice ran out up to 7 km, covering 8–9 km² and reaching the inland Aru co lake. Nine herders were killed along with hundreds of their animals. Surprisingly, a second glacier collapsed (termed Aru-2) at the same region 2.4 km southeast of the Aru-1 just 2 months later, on 21 September 2016 (Fig. 2), from 5800–5240 m a.s.l. in two flows at about 5:00 and 11:20 (Beijing time, UTC+8). It also fragmented and became a mass flow that ran out up to 5 km and covered about 7 km² (Tian et al. 2017; Kääb et al. 2018; Gilbert et al. 2018). From the Google Earth image after the Aru ice avalanches, there was obvious erosion during movement, especially in the gorge area (Fig. 2). Combining Gilbert et al.'s (2018) field investigations and the Google Earth image (of

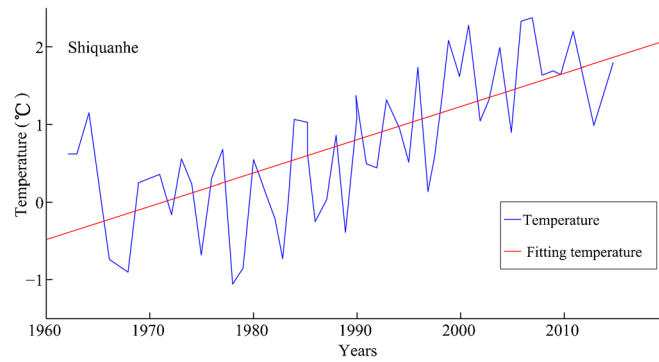


Fig. 1 Annually averaged temperature at the Shiquanhe Meteorological Station (32.50°N, 80.10°E, 4260 m a.s.l.) that is the nearest state-run meteorological station around the Aru Glacier from 1961 to 2015, the red line is the fitting line of annual average temperature (data from Tian et al. 2017)

2017.02.27), those two glaciers flowed on a soft, fine-grained, and highly erodible sedimentary base that possessed large amounts of till, rich in clay/silt with low friction angle. Prior to the Aru avalanches, crevasses were found on satellite imagery (Gilbert et al. 2018; Zhang et al. 2018), which may be caused by force balance evolution within Aru glacier on the detachment zone (Gilbert et al. 2018).

There is a lack of direct observation data to connect the Aru ice avalanches with local climate change. Quincey et al. (2011) suggests that recent climate warming has facilitated glacier surging in the Karakoram Mountains. During the period before the glacier collapses, there was a significant amount of precipitation (Fig. 3) in the region. This could increase the accumulation of liquid water and pore-water pressure, decreasing the basal friction under the glacier which may have led to the eventual occurrence of the twin Aru collapses (Kääb et al. 2018; Gilbert et al. 2018).

Data and methods

Seismic signals and inversion

Long-period seismic waves can be generated by the large-scale acceleration and deceleration of the gravitational mass flows (e.g., landslide and rock-ice avalanches) during their emplacement. Of course, the seismic waves in this paper generated by Aru avalanches have been confirmed. Considering that the wavelength of long-period seismic waves is larger than the spatial scale of the gravitational mass flows; according to theory, the force acting on the Earth's surface produced by the mass flows can be approximated as a single-force mechanism (Fukao 1995; Allstadt 2013; Ekström and Stark 2013; Chao et al. 2016; Zhang et al. 2019). In addition, the long-period seismic waves attenuate very slowly, so that they can be recorded at hundreds and even thousands of kilometers from their source. Considering that there are few

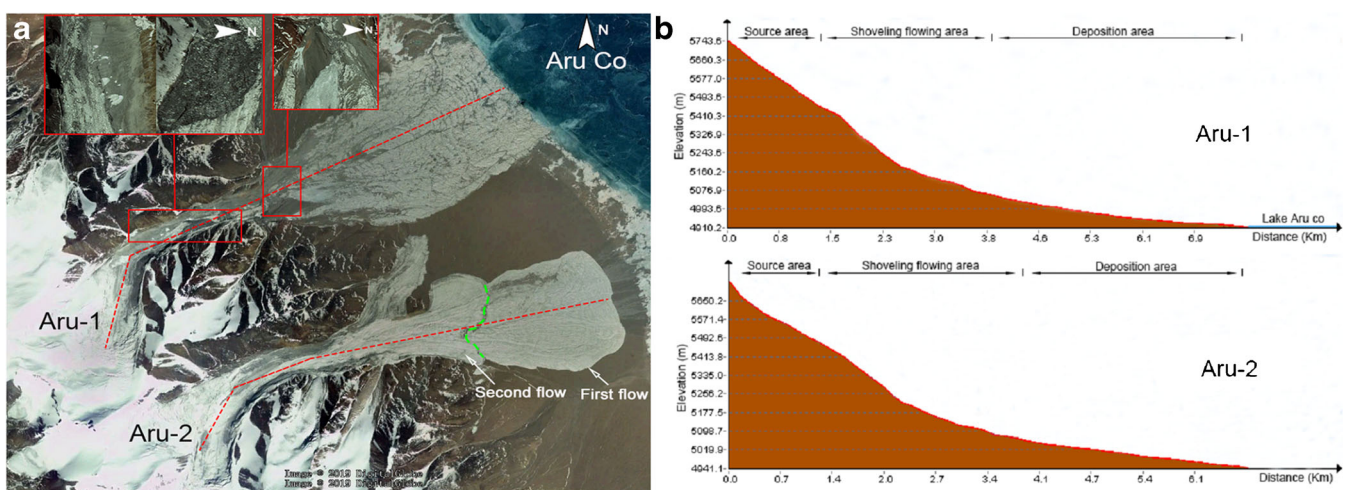


Fig. 2 Google Earth image acquired on 27 February 2017 and profile of the Aru glacier collapses. **a** The red dash lines are the profiles location of Aru glacier collapses (inserts, the left image is a magnification of the erosion section, the right image is a hill similar to the sheep's back stone). **b** Longitudinal profiles of the Aru glacier collapses that could be roughly divided into three sections, i.e., source area, shoveling flowing area, and deposition area

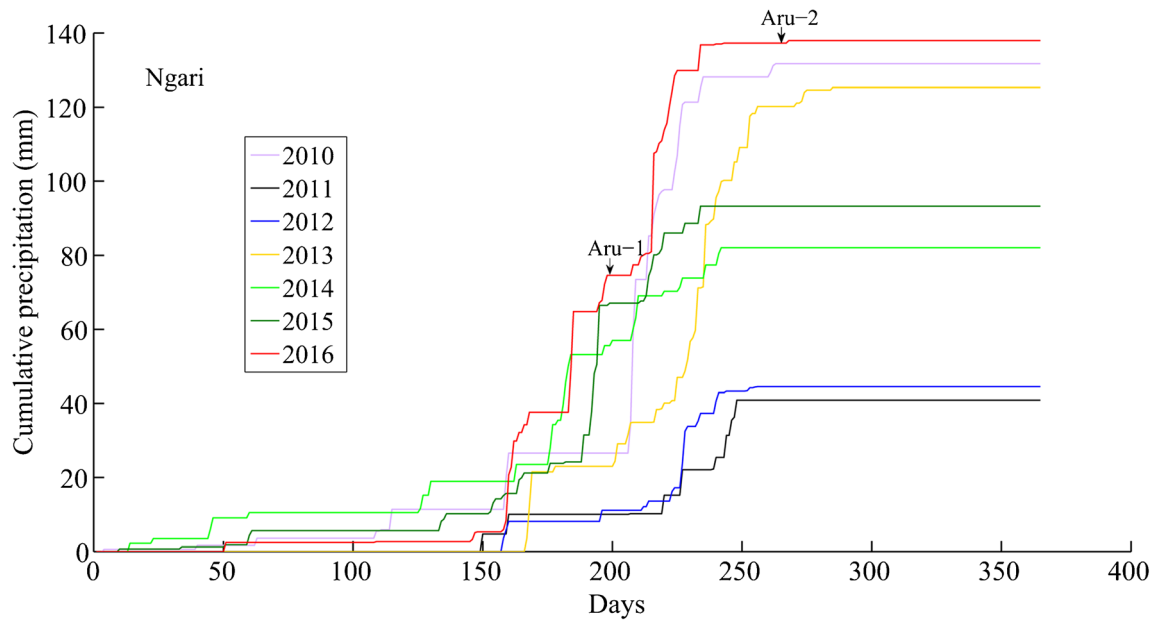


Fig. 3 Daily cumulative precipitation amount at Ngari Meteorological Station (33.39°N, 79.70°E, 4260 m a.s.l.) from 2010 to 2016 and the black arrows represent the dates of the collapse of Aru-1 and Aru-2 (data from <https://doi.org/10.11888/AtmosphericPhysics.tpe.62.db>)

seismic stations close to the Aru area, this paper uses seismic stations from within 500 km of the site where the ice avalanches occurred and where the seismic data could be downloaded from the Data Management Centre of China National Seismic Network at Institute of Geophysics, China Earthquake Administration (Fig. 4). Moreover, the ground-shaking magnitude produced by the Aru ice avalanche movement was relatively small, with the result that identifying the original seismic waveforms produced by the Aru avalanches was difficult. Therefore, it is necessary to design a band-pass filter and Hanning window to remove the interference in low and high frequency bands and obtain long-period signals (38–100 s). Subsequently, seismic signals were processed by removing instrument response, rotating the horizontal components to the radial and transverse directions for each station, and integrating ground velocity to ground displacement.

Long-period seismic waves are insensitive to the small-scale heterogeneity of the Earth's structure because of their long wavelengths. Therefore, simplified Earth velocity models were used in this paper, for example, the 1-D ak135 Earth velocity. Combining the 1-D ak135 Earth velocity with an elastic attenuation model (Kennett et al. 1995), Green's function can be calculated by the matrix propagation method (Wang 1999). The ground displacement recorded by a given station was treated as the convolution of the time series of force vectors in the source area with Green's function, so the force-time function (F) in the time domain could be inverted by a damped least-squares approach to deconvolve Green's function with seismic waves (Allstadt 2013):

$$F = (G^T G + \alpha I)^{-1} G^T d \quad (1)$$

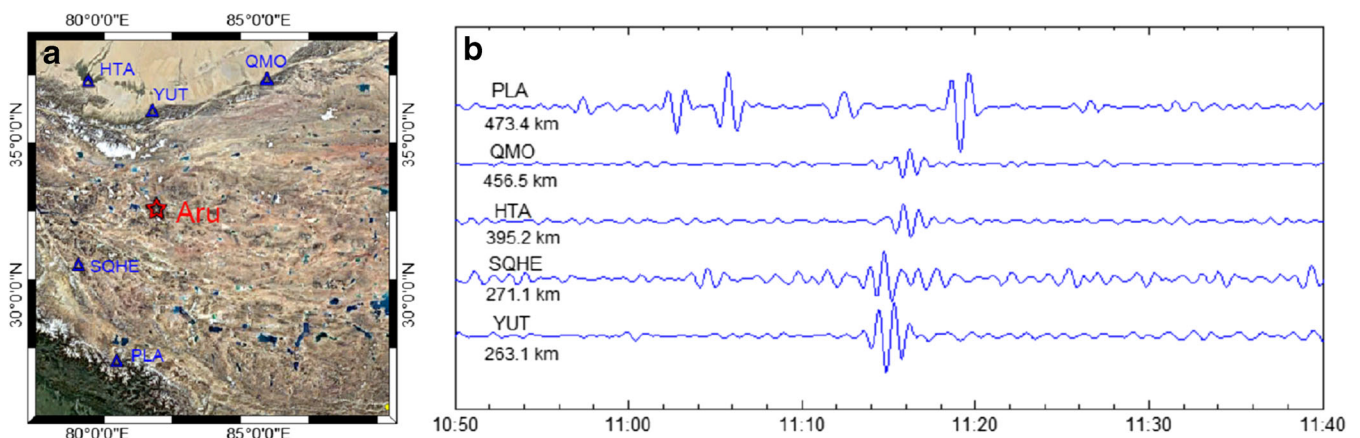


Fig. 4 a The map shows the location of the Aru ice avalanches and seismic stations. b Seismic signals recorded by seismic stations around the Aru-1 ice avalanche in (a)

where G represents the Green's function convolution matrix, T indicates the transpose, I is the identity matrix, and the damping parameter is chosen as the trade-off between keeping the model small while still fitting the data well. This F is the opposite force (F_m) acting on the gravitational mass flows. According to F_m , sliding displacement (L), and the sliding time (t), the mass and friction parameter can be estimated to provide the parameters for later detailed numerical simulation.

Ice-avalanche simulation

Digital elevation model (DEM) data of the pre-collapse topography (30 × 30 m) were downloaded from Geospatial Data Cloud, and the original data were resampled (10 × 10 m) to improve the resolution of the avalanche simulation. The basal topography was represented by $Z(x,y)$ in the Cartesian horizontal-vertical form:

$$\zeta(x,y) = \begin{pmatrix} x \\ y \\ Z(x,y) \end{pmatrix} \tag{2}$$

Tangent vectors of a topographic surface T_x and T_y , were defined by the basal topography, $Z(x,y)$, and projected onto the x,y -plane paralleling the x and y axis, respectively. $T_z(x,y)$ was perpendicular to the surface (+ve upward). According to the procedure in Christen et al. (2010), the vector triad was defined as follows:

$$\begin{aligned} T_x &= \frac{1}{\sqrt{1 + \partial_x Z^2}} \begin{pmatrix} 1 \\ 0 \\ \partial_x Z \end{pmatrix} \\ T_y &= \frac{1}{\sqrt{1 + \partial_y Z^2}} \begin{pmatrix} 0 \\ 1 \\ \partial_y Z \end{pmatrix} \\ T_z &= \frac{1}{\sqrt{1 + \partial_x Z^2 + \partial_y Z^2}} \begin{pmatrix} \partial_x Z \\ \partial_y Z \\ -1 \end{pmatrix} \end{aligned} \tag{3}$$

Therefore, the local components of the gravitational acceleration were expressed based on the surface induced directions (T_x, T_y, T_z)

$$g_x = T_x \cdot g_0 \quad g_y = T_y \cdot g_0 \quad g_z = T_z \cdot g_0 \tag{4}$$

where $g_0 = (0,0,-g)^T$, “ \cdot ” expresses the dot product, and g_x, g_y , and g_z are the components of the gravitational acceleration along the directions of x, y , and z , respectively (Fig. 5).

Because the characteristic length in the flow direction is much larger than its thickness, the long-wave scaling argument has been widely used in the derivation of continuum flow models for gravitational mass flows (Savage and Hutter 1989; Iverson and Denlinger 2001; Mangeney-Castelnau et al. 2003; Christen et al. 2010; Mahboob et al. 2015). A system of one dimensional depth-averaged equations has been derived by Savage and Hutter (1989), and this model has been extended to realistic topographies and higher dimensions (Pudasaini et al. 2005; Pudasaini and Hutter 2007; Fischer et al. 2012). Therefore, we describe the depth-averaged mass and momentum conservation equations involving the characteristics of the Aru ice avalanches during movement (e.g., entrainment) that are given below:

$$\frac{\partial h}{\partial t} + \frac{\partial hu}{\partial x} + \frac{\partial hv}{\partial y} = E \tag{5}$$

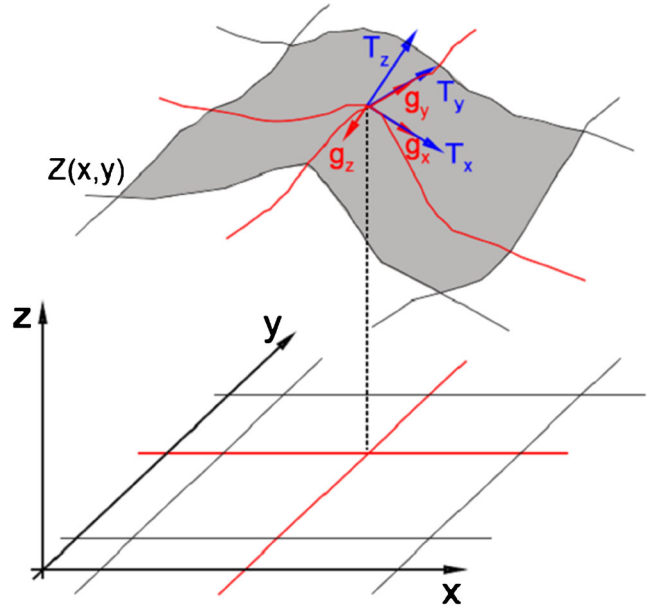


Fig. 5 The topography of a surface given in a Cartesian coordinate system x, y, z , and the z axis is vertically upward. The vector triad (T_x, T_y, T_z) is induced by the topography of a surface and the local components of the gravitational acceleration system are expressed as the vector triad $g = (g_x, g_y, g_z)$ in the direction of the surface induced the vector triad (T_x, T_y, T_z)

$$\frac{\partial hu}{\partial t} + \frac{\partial (hu^2 + \frac{1}{2}k_{ap}g_z h^2)}{\partial x} + \frac{\partial huv}{\partial y} = S_{gx} - S_{fx} - S_{rx} + u_b E. \tag{6}$$

$$\frac{\partial hv}{\partial t} + \frac{\partial huv}{\partial x} + \frac{\partial (hv^2 + \frac{1}{2}k_{ap}g_z h^2)}{\partial y} = S_{gy} - S_{fy} - S_{ry} + v_b E. \tag{7}$$

where E denotes the mass production source term, referred to as the ice-avalanche entrainment rate. The right-hand side terms of the momentum conservation Eqs. (6) and (7) are the external forces. More detailed expressions are as follows:

$$S_{gi} = g_i h \tag{8}$$

$$S_{fi} = \frac{(\tau_b)_i}{\rho} \tag{9}$$

$$S_{ri} = k_{ap} g_z h \frac{\partial Z}{\partial x_i} \tag{10}$$

where g_x, g_y , and g_z are components of gravitational acceleration in the x, y , and z directions, respectively; h is the ice avalanche height; u and v are the velocities in the x and y directions, respectively; ρ is the density of the ice avalanche; $i \in [x, y]$ expressed as the components of the external forces S_{gi}, S_{fi} , and S_{ri} in the x and y directions denoting the gravity force, the basal erosion force, and the lateral pressure, respectively; k_{ap} is the lateral-pressure coefficient, and can be described as

$$k_{ap} = 2 \frac{1 \pm [1 - \cos^2 \phi_{int}(1 + \tan^2 \phi_{bed})]^{\frac{1}{2}}}{\cos^2 \phi_{int}} - 1$$

where ϕ_{int} and ϕ_{bed} are the internal and bed friction angles of the flowing material, “+” and “-” correspond to the passive state ($\partial u/\partial x + \partial v/\partial y \leq 0$) and the active state ($\partial u/\partial x + \partial v/\partial y > 0$), respectively. When the material is in an active stress state, the maximum lateral pressure reduces considerably. In another case, when the material is forced to compress laterally, the maximum lateral pressure increases dramatically. In addition, Davies and McSaveney (2002) proposed that fragmentation could be occurring in a granular mass, when there is further lateral stress caused by overburden pressures, which may lead to additional travel of the distal part of the avalanche. Therefore, the lateral pressure coefficient k_{ap} is important in the simulation of fragmentation during movement.

Entrainment

Erosion is a very common phenomenon in the process of gravitational mass flows, which would increase in volume and significantly influence mobility. To study this phenomenon, scholars have proposed different erosion models for erosion during movement in recent years (McDougall and Hungr 2005; Mangeney et al. 2007; Pirulli and Pastor 2012; Iverson 2012; Ouyang et al. 2015; Liu et al. 2015). Considering the entrainment rate, formula must satisfy boundary momentum jump condition, we adopt the entrainment model in Iverson and Ouyang (2015), which can be described as

$$E = \frac{\tau_b - \tau_s}{\rho \sqrt{u^2 + v^2}} \quad (11)$$

where τ_b is the total basal traction from the ice-avalanche flow; τ_s is the total resistance shear stress from the erodible bed. For τ_b and τ_s , they could be used in an extended Voellmy friction model (Christen et al. 2010) and Coulomb friction model, respectively as follows:

$$\begin{aligned} (\tau_b)_i &= \frac{v_i}{\|u\|} (\rho g_z h \tan \phi_{bed} + R_t u^2 + R_c u^2) \\ R_t &= \mu h \frac{u^T K u}{u^2}, R_c = \frac{g}{\xi} \\ \tau_s &= c + \rho(1-s)g_z h \tan \phi_s \end{aligned} \quad (12)$$

$$K = \begin{pmatrix} K_x & K_{xy} \\ K_{xy} & K_y \end{pmatrix} \quad (13)$$

K_x , K_{xy} and K_y in Eq. (13) can be expressed in detail as follows:

$$\begin{aligned} K_x &= \frac{\partial_x^2 Z}{(1 + \partial_x Z^2) \sqrt{1 + \partial_x Z^2 + \partial_y Z^2}} \\ K_{xy} &= \frac{\partial_x \partial_y Z}{\sqrt{1 + \partial_x Z^2} \sqrt{1 + \partial_y Z^2} \sqrt{1 + \partial_x Z^2 + \partial_y Z^2}} \\ K_y &= \frac{\partial_y^2 Z}{(1 + \partial_y Z^2) \sqrt{1 + \partial_x Z^2 + \partial_y Z^2}} \end{aligned}$$

where $v_i = [u, v]^T$, $i \in [x, y]$ is the VS model that splits the total friction into a velocity-dependent “turbulent” and “viscous” friction (friction coefficient ξ) and a velocity independent dry-Coulomb term that is proportional to the normal stress at the granular mass bottom (friction coefficient μ) (Christen et al. 2010); R_t is the resistance parameter relating to the topography of contact surface and the spatial variations of the field variables (velocities and height); c and ϕ_s are the cohesion and friction angle of the bed material and s is a pore-pressure ratio indicating the degree of liquefaction of the bed material; K is the full curvature tensor of the topography (Christen et al. 2010; Moretti et al. 2015), which affects fluid motion characteristics during movement. A WENO-type (weighted essentially non-oscillatory type) finite volume scheme and an HLLC (Harten-Lax-van Leer Contact) approximate Riemann solver (Toro 2001) were adopted to solve Eqs. (5)–(7).

Results

Based on the inversion of seismic waves, the three-dimensional source forces of Aru-1 were obtained (Fig. 6), and the path of the ice avalanche and movement time inferred from seismic waves. The mass of Aru-1 was estimated as about 1.2×10^{10} kg and average friction coefficient estimated at 0.1, which could be used for further detailed study of the process of ice-avalanche movement in simulation. Such low friction is typical of the values of internal friction obtained for high-speed deformation of granular materials in experimental fault rupture, and by back analyses of rock and ice avalanches.

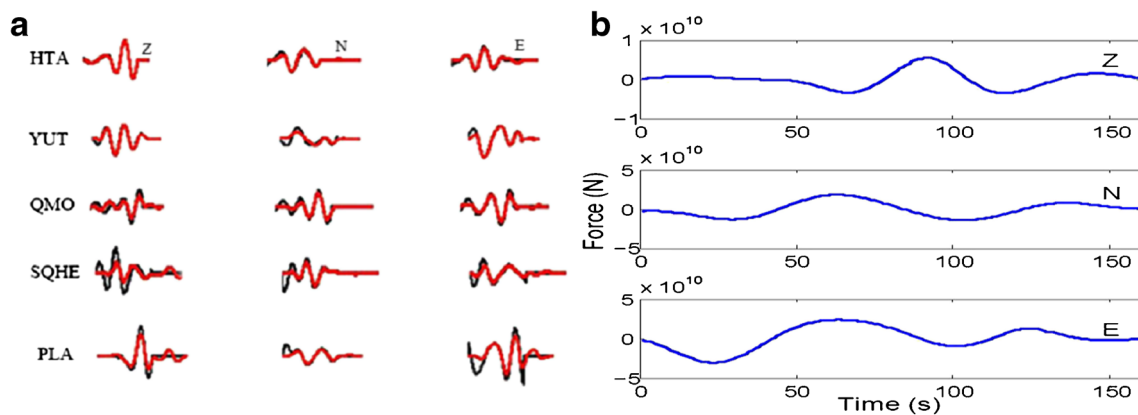


Fig. 6 a Recorded (black lines) and synthetic (red lines) seismograms are compared. Station name is given at the left of each trace. b The three-component force function for the Aru-1 ice avalanche

Combining Google Earth image and Geographic Information System (GIS), we can roughly locate the source area and assign a source mass according to our inversion in the absence of post-event digital elevation terrain data. Owing to the existence of erosion and water content in the eroded layer during the movement process, the dynamic model should consider this situation. In order to simplify the model, we do not consider the water generated by frictional heat in this paper. As the influence of terrain curvature on flow is considered in the model, the phenomenon of the super elevation which occurred at 5 s around the corner (Fig. 7) which is mainly caused by the centrifugal force. The low friction led to high-speed movement of the ice avalanche, estimated as up to 92 m/s in the canyon section. This phenomenon of high-speed motion is also supported by evidence from the hard bedrock protruding at the exit of the glacier that is similar to a roche moutonnée. Here, grassy vegetation on its back has survived the passage of the avalanche, which indicates that a part of the ice avalanche was in high-speed oblique projectile motion (Fig. 7) as it passed over the protruding bedrock. After about 160 s, the front of the Aru-1 ice avalanche rushed into the Aru co lake at about 7 m/s and generated an impact wave which eventually surged to the opposite shore of Aru co lake.

For Aru-2 ice avalanche, the methods are adopted as in Aru-1. Considering that the received poor quality of seismic wave signals produced by the Aru-2 event, however, the volume and friction coefficients of Aru-2 refer to Kääb et al. (2018), where the total volumes of source area and friction coefficients of Aru-2 are about $83 \times 10^6 \text{ m}^3$ (inferred from the pre- and post-event DEMs) and 0.14 ± 0.05 , respectively. For Aru-2, there were two ice avalanches. Although the two ice avalanches occurred less than 1 day apart and

we do not have image data from the time of occurrence, we were still able to identify historical information from the geomorphic form of the deposition body (Shugar and Clague 2011). Based on the TerraSAR-X radar image acquired 3 days after the collapse (24 September 2016), in Kääb et al. (2018) supplementary image and Google Earth image acquired on 27 February 2017, the first and the second Aru-2 ice avalanche flows could be clearly distinguished (Fig. 8). According to Fig. 8b, there is a tributary of an ice-avalanche deposit and a large amount of erosion accumulation at the bottom of the interface, but there is very little in the front of the deposit. By carefully examining the topography, we also could find that the ice avalanche crossed the shoulder of the valley after passing through the low-lying terrain. We reason that because of the deposition of the first ice avalanche, the depth of the canyon had become shallower when the second collapse of Aru-2 flowed through a narrow, shallower valley section in a short time, it would inevitably run over the valley shoulder. And the sliding of the first ice avalanche may have caused the soil at the bottom to become loose, so that the erosion during the second ice avalanche movement may have been more obvious.

Although the boundaries between the two ice avalanches were obvious, we still only know the total volume of the source area of Aru-2. In order to study the characteristics of the process of avalanche movement, we need to roughly calculate the respective volumes of two ice avalanches. For the first ice avalanche of Aru-2, the ratio of drop height to horizontal distance is low, that means the friction coefficient is small and the sliding speed is fast, while the primary ice avalanche process was still nearly undetectable, but the second was recorded by the present seismic network. These may be due to the amount of source material not being

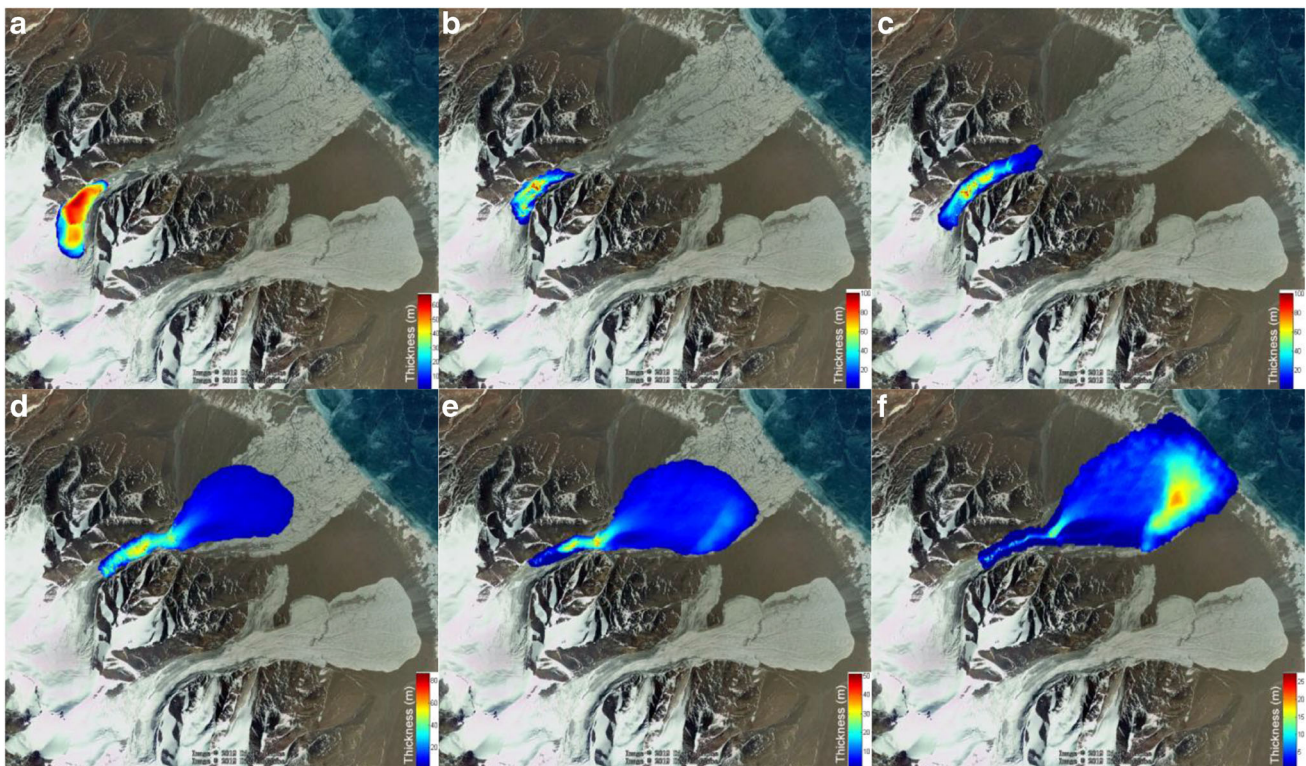


Fig. 7 Simulated the Aru-1 ice avalanche flow depths at different output times, from left to right and then top to bottom $t = 5 \text{ s}, 20 \text{ s}, 40 \text{ s}, 80 \text{ s}, 120 \text{ s}, 160 \text{ s}$

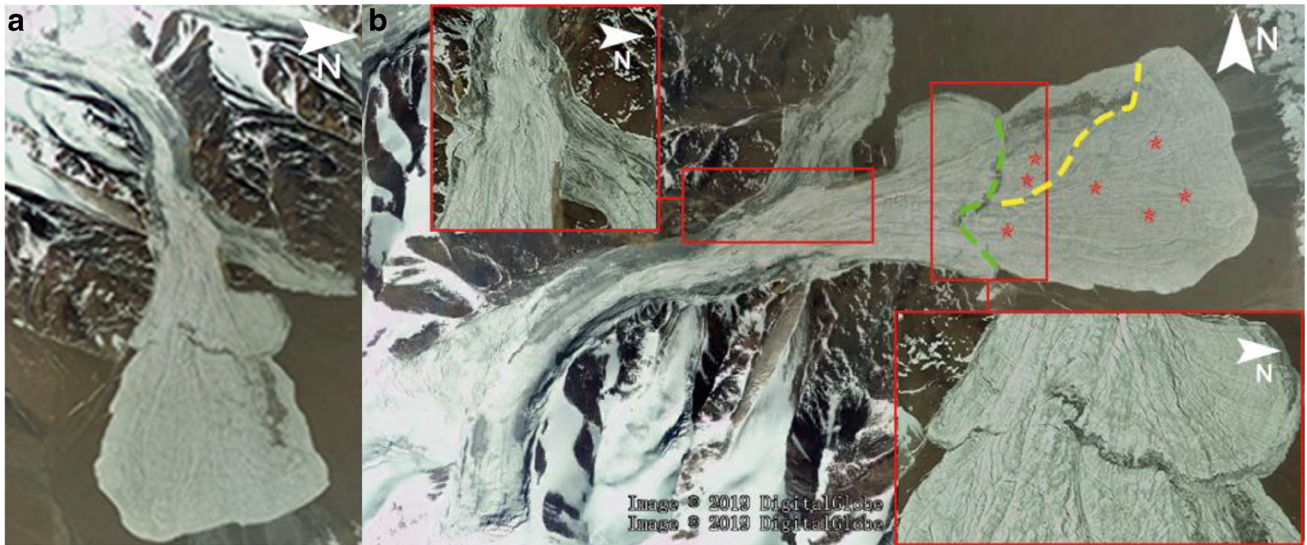


Fig. 8 a The front view of Aru-2 image from Google Earth acquired on 27 February 2017. b This picture is a top view of the Aru-2 collapses (inserts, the left image is a magnified view of the ice avalanche flow over the valley shoulder section; the right image is a magnified view of the boundaries between the first and second collapses. The green line and the yellow line represent the boundary between the first and second collapses and the distinct steps of the first deposit thickness of Aru-2, respectively; the red stars represent the sample points for the depth calculation of the first ice avalanche deposition)

large enough to evoke strong ground vibration; therefore, there is reason to believe that the volume of the first ice avalanche was smaller than that of the second avalanche. Owing to the lack of elevation terrain data after the first ice avalanche of Aru-2, the volume of the first ice avalanche was estimated by comparing the elevation changes of the same sample points after the occurrence of the Google image (2017.02.27) and the terrain elevation data before the event (Fig. 8b). The average difference in elevation was about 4–5 m and the deposition area of the first avalanche was about $4.3 \times 10^6 \text{ m}^2$. In addition, considering the melting of ice, we take the volume of the first avalanche as about $22 \times 10^6 \text{ m}^3$. For the volume of the second avalanche, due to the deposition of ice avalanche in the process of movement, the amount of material inverted from the seismic wave is smaller than that compared with landslides. In this situation, we would also like to verify the effect on the shape of final deposition if we underestimate the amount of material. Therefore, we take the volume of the second avalanche as

about $50 \times 10^6 \text{ m}^3$. The friction coefficient adopted in the first ice avalanche is taken by the ratio of drop height to horizontal distance and add its final deposition (Fig. 9) to the original terrain as the landform over which the second ice avalanche slid. Owing to the deposition along the path, the second ice avalanche flowed on the surface of the first ice avalanche. Therefore, for the second ice avalanche movement, a low friction coefficient should be considered in simulating the second ice avalanche of Aru-2 (Fig. 10).

Discussion and conclusion

A huge mass of glacier first collapsed (Aru-1) on 17 July 2016, in a remote district on the western Tibetan Plateau. A second glacier collapsed (Aru-2) in the same region just 2.4 km southeast of the Aru-1 66 days later. Because of the sudden occurrence of ice avalanches and their location in sparsely populated areas, the characteristics of their movement process were only directly recorded as seismic waves. Major parameters of ice avalanche

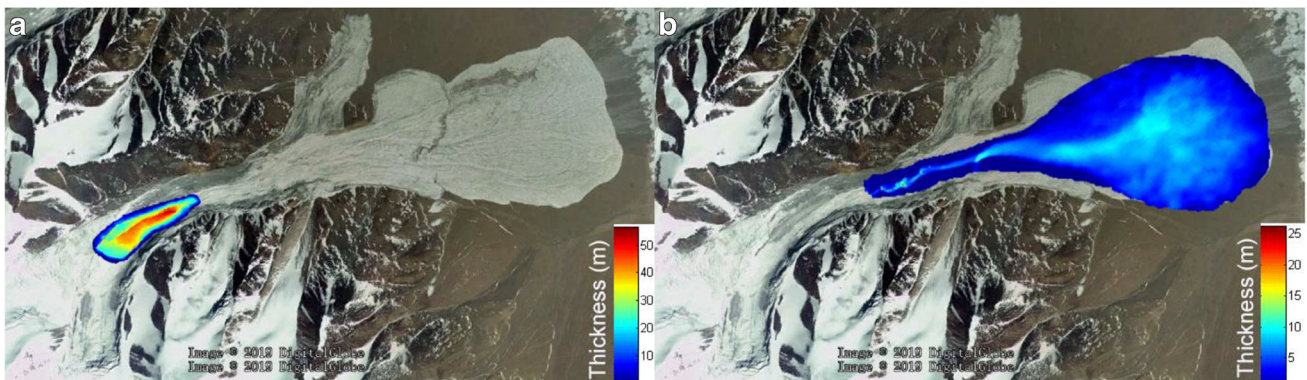


Fig. 9 Simulated the Aru-2 first ice avalanche flow depths. a and b are the beginning and the final deposition forms of Aru-2 first ice avalanche, respectively

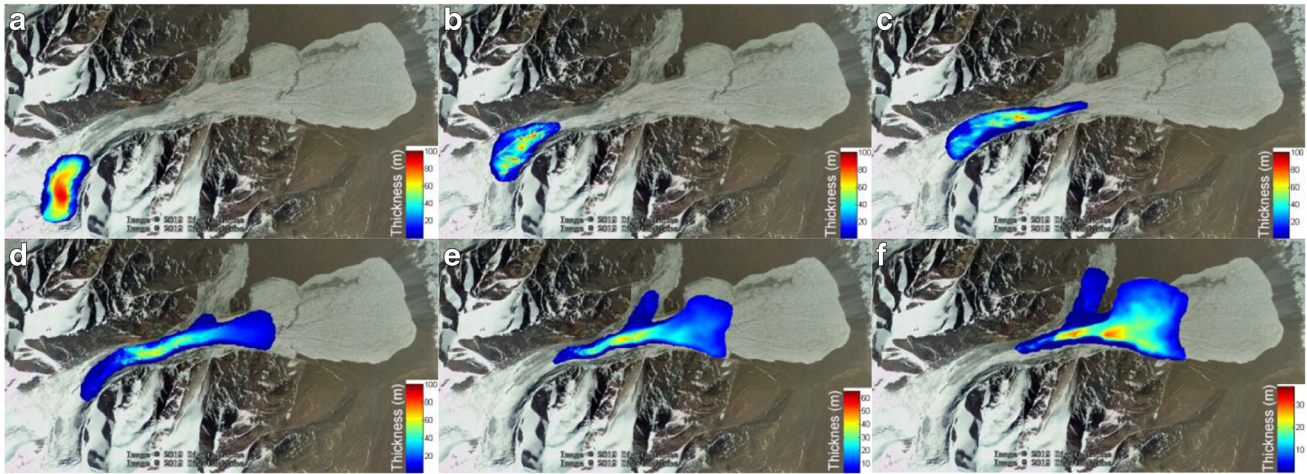


Fig. 10 Simulated the Aru-2 second ice avalanche flow depths at different output times, from left to right and then top to bottom $t = 5$ s, 20 s, 40 s, 80 s, 120 s, 160 s

movement were provided by seismic-wave inversion, which were then used in numerical simulation. However, there were still some shortcomings: (1) the magnitude of the event and the signal-to-noise ratio of the seismic signal are critical to signal generation and inversion, which ultimately leads to whether we can use seismic-wave inversion to provide parameters for numerical simulation; (2) the internal friction angles of the flow material and erosion layer have use estimated values before detailed field investigation; (3) the accuracy of the topographic data before the collapse is low and may affect the results of the numerical simulation; (4) we use Google Earth images and geographic information systems to assign approximate depths of the source area, and the underestimate of the material inverted by seismic wave have some effect on the simulation process, but the facts show that the effect on the deposition state is not obvious and would still be useful for determining the scope of the disaster; (5) the physical model of motion in this paper also needs to be further developed, such as perhaps considering frictional heating leading to ice melting and solid-liquid two-phase interaction of Aru-1 avalanche entering the Aru co lake.

Although numerical simulations use the approximate mass and friction coefficients of ice avalanches inverted from seismic wave, the results of the simulation model are generally consistent with the inversion velocity and the morphology of the deposits. This means that even if we do not know the exact volume or mass of the ice collapse source area, we can still simulate the avalanche process by combining seismic-wave inversion and numerical simulation. Especially for the lack of on-site data in the remote areas, combining numerical simulation with seismic-wave inversion provides the possibility of rapid assessment of potential fatalities after disasters.

Acknowledgments

We thank for the suggestions of anonymous reviewers and Professor Mauri Mcsaveney for assisting in the improvement of the manuscript, which greatly improved the quality of this paper. We also are thankful for the seismic data of this study provided by Data Management Centre of China National Seismic Network at Institute of Geophysics, China Earthquake Administration and the Digital

Elevation Model (DEM) data of pre-collapse which were obtained from the Geospatial Data Cloud (<http://www.gscloud.cn/>).

Funding information This work was supported by the National Key Research and Development Program of China (Project No. 2017YFC1501003), the Major Program of the National Natural Science Foundation of China (Grant No. 41790433), the National Natural Science Foundation of China (Grant No. 41772312), Key Deployment Project of CAS:KFZD-SW-424.

References

- Allstadt K (2013) Extracting source characteristics and dynamics of the August 2010 Mount Meager landslide from broadband seismograms. *J Geophys Res Earth Surf* 118(3):1472–1490
- Bai X, Jian J, He S, Liu W (2019) Dynamic process of the massive Xinmo landslide, Sichuan (China), from joint seismic signal and morphodynamic analysis. *Bull Eng Geol Environ* 78(5):3269–3279. <https://doi.org/10.1007/s10064-018-1360-0>
- Brodsky EE, Gordeev E, Kanamori H (2003) Landslide basal friction as measured by seismic waves. *Geophys Res Lett* 30(24)
- Chao WA, Zhao L, Chen SC, Wu YM, Chen CH, Huang HH (2016) Seismology-based early identification of dam-formation landquake events. *Sci Rep* 6:19259
- Christen M, Kowalski J, Bartelt P (2010) RAMMS: Numerical simulation of dense snow avalanches in three-dimensional terrain. *Cold Reg Sci Technol* 63(1-2):1–14
- Cole SE, Cronin SJ, Sherburn S, Manville V (2009) Seismic signals of snow-slurry lahars in motion: 25 September 2007, Mt Ruapehu, New Zealand. *Geophys Res Lett* 36:L09405. <https://doi.org/10.1029/2009GL038030>
- Davies TR, McSaveney MJ (2002) Dynamic simulation of the motion of fragmenting rock avalanches. *Can Geotech J* 39(4):789–798
- Davies TR, McSaveney MJ, Hodgson KA (1999) A fragmentation-spreading model for long-runout rock avalanches. *Can Geotech J* 36(6):1096–1110
- Duan A, Xiao Z (2015) Does the climate warming hiatus exist over the Tibetan Plateau? *Sci Rep* 5:13711. <https://doi.org/10.1038/srep13711>
- Dufresne A, Wolken GJ, Hibert C et al (2019) The 2016 Lamplugh rock avalanche Alaska: deposit structures and emplacement dynamics. *Landslides* 1–19. <https://doi.org/10.1007/s10346-019-01225-4>.
- Ekström G, Stark CP (2013) Simple scaling of catastrophic landslide dynamics. *Science* 339(6126):1416–1419
- Favreau P, Mangeney A, Lucas A, Crosta G, Bouchut F (2010) Numerical modeling of landquakes. *Geophys Res Lett* 37(15)
- Fischer JT, Kowalski J, Pudasaini SP (2012) Topographic curvature effects in applied avalanche modeling. *Cold Reg Sci Technol* 74:21–30

- Fukao Y (1995) Single-force representation of earthquakes due to landslides or the collapse of caverns. *Geophys J Int* 122(1):243–248. <https://doi.org/10.1111/j.1365-246X.1995.tb03551.x>
- Gilbert A, Leinss S, Kargel J et al (2018) Mechanisms leading to the 2016 giant twin glacier collapses, Aru Range, Tibet. *Cryosphere* 12(9):2883–2900
- Huggel C, Caplan-Auerbach J, Waythomas CF, Wessels RL (2007) Monitoring and modeling ice-rock avalanches from ice-capped volcanoes: a case study of frequent large avalanches on Iliamna Volcano, Alaska. *J Volcanol Geotherm Res* 168(1–4):114–136
- Iverson RM (2012) Elementary theory of bed-sediment entrainment by debris flows and avalanches. *J Geophys Res* 117(F03006). <https://doi.org/10.1029/2011JF002189>
- Iverson RM, Denlinger RP (2001) Flow of variably fluidized granular masses across three-dimensional terrain: 1. Coulomb mixture theory. *J Geophys Res Solid Earth* 106(B1):537–552
- Iverson RM, Ouyang C (2015) Entrainment of bed material by Earth-surface mass flows: review and reformulation of depth-integrated theory. *Rev Geophys* 53:27–58. <https://doi.org/10.1002/2013RG000447>
- Kääb A et al (2005) Remote sensing of glacier-and permafrost-related hazards in high mountains: an overview. *Nat Hazards Earth Syst Sci* 5:527–554. <https://doi.org/10.5194/nhess-5-527-2005>
- Kääb A, Leinss S, Gilbert A et al (2018) Massive collapse of two glaciers in western Tibet in 2016 after surge-like instability. *Nat Geosci* 11(2):114
- Kennett BLN, Engdahl ER, Buland R (1995) Constraints on seismic velocities in the Earth from traveltimes. *Geophys J R Astron Soc* 122(1):108–124
- Li Z, Huang X, Xu Q, Yu D, Fan J, Qiao X (2017) Dynamics of the Wulong landslide revealed by broadband seismic records. *Earth Planet Space* 69(1):27
- Li W, Chen Y, Liu F, Yang H, Liu J, Fu B (2019) Chain-style landslide hazardous process: constraints from seismic signals analysis of the 2017 Xinmo landslide, SW China. *J Geophys Res: Solid Earth* 124. <https://doi.org/10.1029/2018JB016433>
- Liu X, Chen B (2000) Climatic warming in the Tibetan Plateau during recent decades. *Int J Climatol* 20:1729–1742. [https://doi.org/10.1002/1097-0088\(20001130\)20:14<1729::AID-JOC556>3.0.CO;2-Y](https://doi.org/10.1002/1097-0088(20001130)20:14<1729::AID-JOC556>3.0.CO;2-Y)
- Liu W, He S, Li X (2015) Numerical simulation of landslide over erodible surface. *Geoenviron Disasters* 2(1):19
- Mahboob MA, Iqbal J, Atif I (2015) Modeling and simulation of glacier avalanche: a case study of Gayari sector glaciers hazards assessment. *IEEE Trans Geosci Remote Sens* 53(11):5824–5834
- Mangeney A, Tsimring LS, Volfson D, Aranson IS, Bouchut F (2007) Avalanche mobility induced by the presence of an erodible bed and associated entrainment. *Geophys Res Lett* 34(22)
- Mangeney-Castelnau A, Vilotte JP, Bristeau MO, Perthame B, Bouchut F, Simeoni C, Yerneni S (2003) Numerical modeling of avalanches based on Saint Venant equations using a kinetic scheme. *J Geophys Res Solid Earth* 108(B11)
- McDougall S, Hungr O (2005) Dynamic modelling of entrainment in rapid landslides. *Can Geotech J* 42(5):1437–1448
- McSaveney MJ (2002) Recent rockfalls and rock avalanches in Mount Cook national park, New Zealand. *Rev Eng Geol* 15:35–70
- McSaveney MJ, Davies TR (2007) Rockslides and their motion. In: Sassa K, Fukuoka H, Wang F, Wang G (eds) *Progress in landslide science*. Springer-Verlag, Berlin, pp 113–134. https://doi.org/10.1007/978-3-540-70965-7_8
- Moretti L, Mangeney A, Capdeville Y, Stutzmann E, Huggel C, Schneider D, Bouchut F (2012) Numerical modeling of the Mount Steller landslide flow history and of the generated long period seismic waves. *Geophys Res Lett* 39(16)
- Moretti L, Allstadt K, Mangeney A, Capdeville Y, Stutzmann E, Bouchut F (2015) Numerical modeling of the Mount Meager landslide constrained by its force history derived from seismic data. *J Geophys Res Solid Earth* 120:2579–2599. <https://doi.org/10.1002/2014JB011426>
- Ouyang C, He S, Tang C (2015) Numerical analysis of dynamics of debris flow over erodible beds in Wenchuan earthquake-induced area. *Eng Geol* 194:62–72
- Pirulli M, Pastor M (2012) Numerical study on the entrainment of bed material into rapid landslides. *Geotechnique* 62(11):959–972
- Pudasaini SP, Hutter K (2007) *Avalanche dynamics: dynamics of rapid flows of dense granular avalanches*. Springer, Berlin
- Pudasaini SP, Wang Y, Hutter K (2005) Modelling debris flows down general channels. *Nat Hazards Earth Syst Sci* 5(6):799–819
- Quincey DJ, Braun M, Glasser NF, Bishop MP, Hewitt K, Luckman A (2011) Karakoram glacier surge dynamics. *Geophys Res Lett* 38(18)
- Sabot F, Naaim M, Granada F, Surinach E, Planet P, Furdada G (1998) Study of avalanche dynamics by seismic methods, image-processing techniques and numerical models. *Ann Glaciol* 26:319–323
- Savage SB, Hutter K (1989) The motion of a finite mass of granular material down a rough incline. *J Fluid Mech* 199:177–215
- Schneider JF (2004) Risk assessment of remote geohazards in western Pamir, GBAO, Tajikistan. In: *Proceedings of the international conference on high mountain hazard prevention, Vladikavkaz Moscow, 23–26.06. 2004*, pp 252–255.
- Schneider D, Bartelt P, Caplan-Auerbach J, Christen M, Huggel C, McArdell BW (2010) Insights into rock-ice avalanche dynamics by combined analysis of seismic recordings and a numerical avalanche model. *J Geophys Res Earth* 115. <https://doi.org/10.1029/2010JF001734>
- Schneider D, Huggel C, Haeblerli W, Kaitna R (2011) Unraveling driving factors for large rock-ice avalanche mobility. *Earth Surf Process Landf* 36(14):1948–1966
- Shugar DH, Clague JJ (2011) The sedimentology and geomorphology of rock avalanche deposits on glaciers. *Sedimentology* 58(7):1762–1783. <https://doi.org/10.1111/j.1365-3091.2011.01238.x>
- Sosio R, Crosta GB, Hungr O (2008) Complete dynamic modeling calibration for the Thurwieser rock avalanche (Italian Central Alps). *Eng Geol Amst* 100:11–26. <https://doi.org/10.1016/j.enggeo.2008.02.012>
- Tian L, Yao T, Gao Y et al (2017) Two glaciers collapse in western Tibet. *J Glaciol* 63(237):194–197
- Toro EF (2001) *Shock capturing methods for free surface shallow flows*. John Wiley & Sons, Chichester
- Wang R (1999) A simple orthonormalization method for stable and efficient computation of Green's functions. *Bull Seismol Soc Am* 89(3):733–741. Accession: 029788774
- Wang B, Bao Q, Hoskins B, Wu G, Liu Y (2008) Tibetan Plateau warming and precipitation changes in East Asia. *Geophys Res Lett* 35:L14702. <https://doi.org/10.1029/2008GL034330>
- Yamada M, Mangeney A, Matsushi Y, Moretti L (2016) Estimation of dynamic friction of the Akatani landslide from seismic waveform inversion and numerical simulation. *Geophys J Int* 206(3):1479–1486
- Zhang Z, Liu S, Zhang Y et al (2018) Glacier variations at Aru Co in western Tibet from 1971 to 2016 derived from remote-sensing data. *J Glaciol* 64(245):397–406
- Zhang Z, He S, Liu W, et al (2019) Source characteristics and dynamics of the October 2018 Baige landslide revealed by broadband seismograms. *Landslides* 1–9

X. Bai

Institute of Tibetan Plateau Research,
Chinese Academy of Sciences,
Beijing, China

X. Bai · S. He

CAS Center for Excellence in Tibetan Plateau Earth Sciences,
Beijing, China

X. Bai · S. He

University of Chinese Academy of Sciences,
Beijing, China

S. He (✉)

Key Laboratory of Mountain Hazards and Surface Process, Institute of Mountain Hazards and Environment,
Chinese Academy of Sciences,
Chengdu, China
Email: hsm@imde.ac.cn